# NJC

Accepted Manuscript


This is an *Accepted Manuscript*, which has been through the Royal Society of Chemistry peer review process and has been accepted for publication.

*Accepted Manuscripts* are published online shortly after acceptance, before technical editing, formatting and proof reading. Using this free service, authors can make their results available to the community, in citable form, before we publish the edited article. We will replace this *Accepted Manuscript* with the edited and formatted *Advance Article* as soon as it is available.

You can find more information about *Accepted Manuscripts* in the Information for Authors.

Please note that technical editing may introduce minor changes to the text and/or graphics, which may alter content. The journal's standard Terms & Conditions and the Ethical guidelines still apply. In no event shall the Royal Society of Chemistry be held responsible for any errors or omissions in this *Accepted Manuscript* or any consequences arising from the use of any information it contains.

ROYAL SOCIETY OF CHEMISTRY

www.rsc.org/njc

Cite this: DOI: 10.1039/c0xx00000x

www.rsc.org/xxxxxx

**ARTICLE TYPE**

# Thermodecomposition synthesis of porous $\beta$-$Bi_2O_3$/$Bi_2O_2CO_3$ heterostructured photocatalyst with improved visible light photocatalytic activity

**Gangqiang Zhu*[,a], Yongbao Liu[a], Mirabbos Hojamberdiev*[,b], Juanli Han[a], Juan Rodríguez[c], Sara Aldabe Bilmes[d], Peng Liu[a]**

***Received (in XXX, XXX) Xth XXXXXXXXX 20XX, Accepted Xth XXXXXXXXX 20XX***
**DOI: 10.1039/b000000x**

Novel porous $\beta$-$Bi_2O_3$/$Bi_2O_2CO_3$ *p-n* heterostructures were synthesized by partially decomposing porous $Bi_2O_2CO_3$ at 300-375°C. The structures, morphologies, optical properties, and specific surface areas of the as-synthesized samples were characterized by means of thermogravimetry and differential scanning calorimetry, X-ray diffraction, scanning electron microscopy, UV-Vis spectroscopy, and $N_2$ gas adsorption. Two types of dye, methyl orange (MO) and methylene blue (MB), were chosen as model organic pollutants to evaluate the photocatalytic activity of the as-synthesized samples. The porous $\beta$-$Bi_2O_3$/$Bi_2O_2CO_3$ *p-n* heterostructures exhibited much higher photocatalytic activity than $\beta$-$Bi_2O_3$ and $Bi_2O_2CO_3$ and MO and MB could be completely degraded within 24 and 50 min, respectively. In addition, phenol as a colorless organic pollutant was also chosen to further study the photocatalytic activity of $Bi_2O_2CO_3$, $\beta$-$Bi_2O_3$ and $\beta$-$Bi_2O_3$/$Bi_2O_2CO_3$. The $\beta$-$Bi_2O_3$/$Bi_2O_2CO_3$ heterostructures also showed much higher photocatalytic activity for the photodegradation of phenol than $\beta$-$Bi_2O_3$ and $Bi_2O_2CO_3$. The obtained results indicated that the formed *p-n* heterojunction in the porous $\beta$-$Bi_2O_3$/$Bi_2O_2CO_3$ composite significantly contributed to the improvement of electron-hole separation and the enhancement of photocatalytic activity. The mechanisms for the enhanced photodegradation of selected organic pollutants over the $\beta$-$Bi_2O_3$/$Bi_2O_2CO_3$ composite are discussed in this study.

## 1. Introduction

Environmental pollution and energy shortage are today's two major global challenges. Semiconductor-based photocatalysis is considered to be a green technology allowing the utilization of solar light for environmental remediation and solar energy conversion, thus providing a potential route to solve both problems [1,2]. Besides individual semiconductor photocatalysts, the composite photocatalysts with a *p-n* heterojunction have also been intensively studied in recent years [3-5]. Due to the formation of a *p-n* heterojunction that can significantly reduce the recombination and increase the separation rate of photogenerated charge carriers, the composite photocatalysts are photocatalytically more active than the individual counterparts [6-9].

As a member of Aurivillius-related oxide family [10,11], bismuth subcarbonate ($Bi_2O_2CO_3$) has practical applications in pharmaceutical and medical industry [12]. The internal layered structure of $Bi_2O_2CO_3$ can guide the lower growth rate along the (001) axis compared to other axes, forming sheet-like nanostructures with exposed {001} facet. The use of $Bi_2O_2CO_3$ as a photocatalyst was previously reported by Cheng et al. [13] for the degradation of methyl orange (MO) in aqueous solution. The band gap and electronic structure of $Bi_2O_2CO_3$ were investigated by Liu et al. [14] by applying first-principles calculations. However, the wider band gap (2.87–3.58 eV) of $Bi_2O_2CO_3$ photocatalyst restricts its practical applications under visible light.

Considering $Bi_2O_2CO_3$ as an important photocatalyst, its photocatalytic efficiency should be further enhanced in order to make it suitable for practical applications under visible light. In recent years, several approaches, including the controlled synthesis of the facet-exposed nanostructures, the modification with noble metal nanoparticles, and the development of composites with narrow band-gap semiconductors, have been proposed to enhance visible-light-driven photocatalytic activity of $Bi_2O_2CO_3$ for the photodegradation of organic pollutants [15,16].

Zheng et al. [17] reported that the $Bi_2O_2CO_3$ flower-like hierarchitectures with exposed {001} facets showed an admirable photocatalytic activity under visible light. Noble metal (Au, Ag, and Pt) nanoparticles loaded on semiconductors can enhance photocatalytic activity by trapping electrons and thereby hindering the recombination of photo-generated $e^-$-$h^+$ pairs. Peng et al. [18] synthesized Ag/$Bi_2O_2CO_3$ microspheres with a significantly enhanced photocatalytic activity compared with bare $Bi_2O_2CO_3$ for the photodegradation of MO in aqueous solution under UV-vis light. Recently, much research work has focused

on nanostructures and photocatalytic activity of $Bi_2O_2CO_3$ heterostructured with narrow band-gap semiconductors. For instance, Chen et al. [19] fabricated $Bi_2O_2CO_3$/BiOI composite at room temperature, and its excellent photocatalytic efficiency was closely related to the $Bi_2O_2CO_3$/BiOI heterojunction that is regarded to be a favorable factor for the separation of photogenerated electrons and holes. Liang et al. [20] synthesized $Ag_2O/Bi_2O_2CO_3$ *p-n* heterojunction demonstrating higher photocatalytic activity than pure $Bi_2O_2CO_3$. Other nanocomposites, such as $BiVO_4/Bi_2O_2CO_3$ [21], $BiOCl/Bi_2O_2CO_3$ [22], $Bi_2O_2CO_3/Bi_2MoO_6$ [23], $Bi_2O_2CO_3/Bi_2S_3$ [24], $Bi_2O_2CO_3/Bi_2WO_6$ [25], and $Bi_2O_2CO_3/Bi_3NbO_7$ [26], also showed an improved photocatalytic activity than pure $Bi_2O_2CO_3$ nanostructures. A semiconductor coupling not only can broaden light absorption but also can highly separate the photo-generated $e^-$-$h^+$ pairs, resulting in improved photocatalytic activity [3]. Therefore, the fabrication of heterostructures is essential to enhance the photocatalytic activity of $Bi_2O_2CO_3$.

As another member of the bismuth oxide family, bismuth(III) oxide ($Bi_2O_3$) is a *p*-type semiconductor ($E_g$ = 2.3-2.8 eV) with four main crystallographic polymorphs: $\alpha$-, $\beta$-, $\gamma$-, and $\delta$-$Bi_2O_3$ [27]. $Bi_2O_3$ has also been demonstrated as a visible-light-active photocatalyst [28-31]. However, $Bi_2O_3$ shows a relatively low photocatalytic activity due to the fast recombination of photogenerated $e^-$-$h^+$ pairs [32]. Despite its low photocatalytic activity, $Bi_2O_3$ has been widely used as a photosensitizer to absorb visible light and form a *p-n* heterojunction to improve photocatalytic activity of the composite photocatalysts, namely, $BiOCl/Bi_2O_3$ [33], $BiVO_4$@$Bi_2O_3$ [34], $Bi_2O_3$/N-$Bi_3NbO_7$ [35], $Bi_2O_3/BaTiO_3$ [36], $Bi_2O_3/Bi_2WO_6$ [37], etc. Tetragonal $\beta$-$Bi_2O_3$ was reported as an excellent photocatalyst particularly for water treatment under visible light [29,30,38,39]. Considering the formation of $\beta$-$Bi_2O_3/Bi_2O_2CO_3$ *p-n* heterojunction, electrons photo-generated from the VB of $\beta$-$Bi_2O_3$ can be transferred to $Bi_2O_2CO_3$, and electrons can accumulate and form internal micro-electric fields between these two semiconductors, promoting the migration of photo-generated charge carriers and improving the photocatalytic activity under visible light.

In this work, porous $\beta$-$Bi_2O_3/Bi_2O_2CO_3$ composite photocatalyst with highly enhanced photocatalytic activity is fabricated by partially decomposing porous $Bi_2O_2CO_3$ microspheres synthesized by hydrothermal method at 160°C. The excellent photocatalytic activity of composite photocatalyst is evaluated by photodegradation of MO, MB, and phenol under visible light irradiation (> 400 nm). Moreover, various scavengers are also introduced into the photodegradation process of MO to discriminate the contributions of different reactive species, and possible mechanisms for the enhanced photocatalytic activity of $\beta$-$Bi_2O_3/Bi_2O_2CO_3$ composite photocatalyst are also discussed.

## 2. Experimental

### 2.1 Preparation

All chemicals with analytical purity were purchased from Shanghai Chemical Reagent Co., Ltd. (China) and used without further purification. Deionized water was used throughout the experiments. In a typical process, 0.97 g of $Bi(NO_3)_3 \cdot 5H_2O$ was dissolved in 10 mL of 1 M $HNO_3$, and 0.28 g of citric acid was then introduced into the solution. After stirring for 10 min, the pH of the solution was adjusted to 4.2 with the dropwise addition of 0.1 M NaOH aqueous solution. Once the pH of the solution reached 4.2, the milky suspension was immediately formed. The resulting precursor suspension was transferred into a Teflon-lined stainless steel autoclave with a capacity of 70 mL, maintained at 180°C for 24 h, and cooled to room temperature. The precipitate was collected by centrifugation, washed with deionized water and ethanol for several times, and dried at 60°C for 10 h. The hydrothermally synthesized $Bi_2O_2CO_3$ samples were then calcined at 300°C, 310°C, 325°C, 340°C, 350°C, and 375°C for 3 h to fabricate $\beta$-$Bi_2O_3/Bi_2O_2CO_3$ composites. The samples were denoted as S300, S310, S325, S340, S350, and S375 according to their calcination temperatures.

### 2.2 Characterization

The crystalline phases of the samples were identified by X-ray powder diffraction using a D/Max2550 X-ray diffractometer (Rigaku) with Cu K$\alpha$ radiation ($\lambda$ = 1.5406 Å). The powder samples were scanned at a scanning rate of 8°/min in the 2$\theta$ range of 10-80° at 40 kV and 50 mA. The scanning electron microscopic (SEM) images were taken by using an S-4800 field emission scanning electron microscope (Hitachi). Transmission electron microscopy (TEM) and high-resolution transmission electron microscopy (HRTEM) observations were performed by using a JEM-2100F electron microscope (JEOL). The Brunauer–Emmett–Teller (BET) specific surface areas ($S_{BET}$) of the samples were measured by a $N_2$ gas adsorption method using an ASAP 2020 instrument (Micromeritics). The samples were degassed at 120°C for 5 h prior to $N_2$ gas adsorption measurements. The $S_{BET}$ values were obtained by a multipoint BET method using the adsorption data in the relative pressure ($P/P_0$) range of 0.05-0.3. The pore size distribution was calculated by the Barrett, Joyner, and Halenda (BJH) method using the desorption isotherm. The X-ray photoelectron spectroscopy (XPS) analysis was performed on ESCALAB MKII X-ray photoelectron spectrometer (VG Scientific) using Mg K$\alpha$ radiation (1253.6 eV). All the binding energies were normalized with respect to the C 1s signal at 284.6 eV. Ultraviolet-visible (UV-vis) absorbance spectra of the samples were recorded on a PE950 UV-Vis spectrophotometer (Perkin-Elmer) using $BaSO_4$ as a standard sample. The quantitative XRD analysis of $Bi_2O_2CO_3$ and $\beta$-$Bi_2O_3$ in the $\beta$-$Bi_2O_3/Bi_2O_2CO_3$ composite photocatalysts was performed on multi-phase patterns by the RIR method [40-42]. The RIR values of the samples were summarized and recognized by the International Centre for Diffraction Data (ICDD) data. Based on the RIR values, the percentages of $Bi_2O_2CO_3$ and β-$Bi_2O_3$ in the heterostructured photocatalyst can be analyzed by applying the "adiabatic principle" if all components are crystalline and identified [40]. Particularly, when the sample is only consisted of two phases, the RIR values can be read from the PDF database, and the weight ratio of each component can be calculated using the following formula:

$$W_a = I_a/[I_a + (I_b/(RIR_b/RIR_a))] \quad (1)$$

$$W_b = I_b/[I_b + (I_a/(RIR_a/RIR_b))] = 1 - W_a \quad (2)$$

where $W_a$ and $W_b$ are the weight ratios of phase a and b, respectively; $I_a$ and $I_b$ are the integrated intensities of the

strongest peaks of phase a and b, respectively. For $Bi_2O_2CO_3$ and β-$Bi_2O_3$, I values were determined from the (110) peak of $Bi_2O_2CO_3$ and the (100) peak of β-$Bi_2O_3$, respectively.

### 2.3 Photocatalytic activity test

Methyl orange (MO), methylene blue (MB), and phenol were used as anionic dye, cationic dye, and colorless target pollutant, respectively, to evaluate the photocatalytic activity of the synthesized composites. The photodegradation reaction was conducted using a 300W Xe lamp (Institute of Electric Light Source, Beijing) with a 400 nm cut-off filter as a visible light source. First, 0.05 g of composite photocatalyst was dispersed in 50 mL of MO (10 mg/L), MB (10 mg/L), or phenol (0.2 mmol/L) aqueous solutions in a Pyrex glass reactor (with a 30 $cm^2$ cross section and 5 cm height). Prior to irradiation, the suspensions were kept in the dark for 30 min to reach the adsorption-desorption equilibrium. During photodegradation reaction, 2 mL of suspension was taken out at certain time intervals for subsequent MO, MB or phenol concentration analysis. The MO, MB, and phenol concentrations were analyzed after filtration by using a U-3010 UV-vis spectrophotometer (Hitachi).

### 2.4 Study of scavenger's effect

To evaluate the roles of the reactive species during the photodegradation process, different scavengers and $N_2$ purging without any scavengers were employed in the photodegradation of MO. As scavengers, benzoquinone, isopropyl alcohol, and ammonium oxalate were used as traps for $•O^{2-}$, •OH, and $h^+$, respectively. The scavengers were introduced into the MO solution before adding the composite photocatalyst. The final concentrations of benzoquinone, isopropyl alcohol, and ammonium oxalate in the reaction system were 1.0 mmol/L.

### 2.5 Photoelectrochemical characterization

To prepare working electrodes for the detection of transient photocurrent responses, the FTO glass was first ultrasonically cleaned in deionized water, ethanol, and acetone, and the slurry containing 80% composite photocatalyst, 10% acetylene black, and 10% PVDF was drop coated on the surface of the FTO glass and dried in a vacuum oven at 60°C for 10 h. An area of electrode was controlled to be 0.5 × 0.5 $cm^2$. A 300W Xe lamp was used as a light source with a UV-cut filter ($\lambda$ > 400 nm). Amperometric *I-T* curve measurements were performed on a Zennium electrochemical workstation (ZAHNER-Elektrik GmbH & Co. KG) in a three-electrode system with a Pt mesh as a counter electrode, a saturated calomel electrode as a reference electrode, and 0.5 M $Na_2SO_4$ aqueous solution as an electrolyte.

## 3. Results and Discussion

In this study, porous $\beta$-$Bi_2O_3$/$Bi_2O_2CO_3$ composite photocatalysts with a *p-n* heterojunction were synthesized by thermodecomposition of sphere-like $Bi_2O_2CO_3$ hierarchitectures with exposed {001} facets in the temperature range of 300-375°C.

### 3.1 Thermal analysis of the transformation of $Bi_2O_2CO_3$ to $\beta$-$Bi_2O_3$

The TG-DSC curves of the $Bi_2O_2CO_3$ precursor were recorded to understand the formation process of $\beta$-$Bi_2O_3$/$Bi_2O_2CO_3$ heterostructured photocatalyst. In Fig. 1, the TG-DSC curves can be divided into four regions: (I) 30-244°C, (II) 244-366°C, (III) 366-719°C, and (IV) 719-800°C. In region I, there is a mass loss of 1.0% in the temperature range of 30-230°C due to the evaporation of adsorbed water. In region II, an obvious exothermic peak at 278°C and a notable mass loss of 12.48% in the temperature range of 230-368°C can be seen. In this region, majority of $Bi_2O_2CO_3$ transforms to crystalline $\beta$-$Bi_2O_3$ simultaneously. The mass loss of 12.48% is slightly greater than the theoretical value (12.02%) of pure $Bi_2O_2CO_3$, which can be attributed to the removal of citric acid molecules adsorbed on the surface of the $Bi_2O_2CO_3$ crystals. In region III, a small exothermic peak is observed at 454°C without any mass loss due to the transformation of metastable tetragonal $\beta$-$Bi_2O_3$ to stable monoclinic $\alpha$-$Bi_2O_3$ [30]. When the temperature is higher than 454°C, there is only one endothermic peak at 734°C without any mass loss in region IV because of the melting of $\alpha$-$Bi_2O_3$. Therefore, the calcination temperatures in the range of 300-350°C were determined to be suitable for the synthesis of $\beta$-$Bi_2O_3$/$Bi_2O_2CO_3$ composite photocatalysts with different amounts of $\beta$-$Bi_2O_3$.

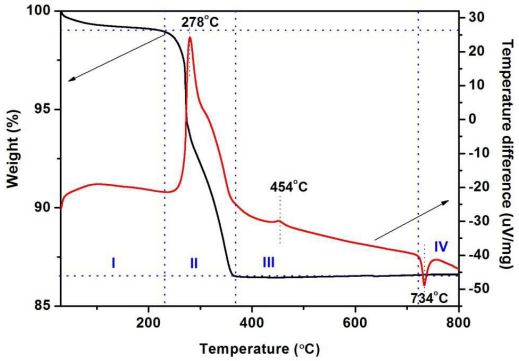


Fig. 1 TG-DSC curves of the $Bi_2O_2CO_3$ precursor

Table 1. Crystallite size (D), specific surface area ($S_{BET}$), pore size, band gap ($E_g$), MO photodegradation rate constant, and $\beta$-$Bi_2O_3$/$Bi_2O_2CO_3$ ratio of the samples

| Sample | $D_1$ (nm) $Bi_2O_2CO_3$ | $D_2$ (nm) $\beta$-$Bi_2O_3$ | $S_{BET}$ ($m^2$/g) | Porous size (nm) | $E_g$ (eV) | $k_1$ (MO) ($min^{-1}$) | Amount of $Bi_2O_2CO_3$ (%) | Amount of $Bi_2O_3$ (%) |
|---|---|---|---|---|---|---|---|---|
| $Bi_2O_2CO_3$ | 26 | – | 32.09 | 15.2 | 3.10 | 0.0218 | 100.0 | 0 |
| S300 | 30 | – | 22.06 | 13.2 | 3.00 | 0.0628 | 81.7 | 18.3 |
| S310 | 28 | 28 | 10.45 | 13.1 | 2.37 | 0.0676 | 54.2 | 45.8 |
| S325 | 24 | 33 | 9.57 | 15.3 | 2.35 | 0.0784 | 32.1 | 67.9 |
| S340 | – | 39 | 8.54 | 15.2 | 2.23 | 0.0482 | 11.5 | 88.5 |
| S350 | – | 41 | 8.41 | 19.2 | 2.21 | 0.0472 | 0 | 100 |

Cite this: DOI: 10.1039/c0xx00000x

www.rsc.org/xxxxxx

ARTICLE TYPE

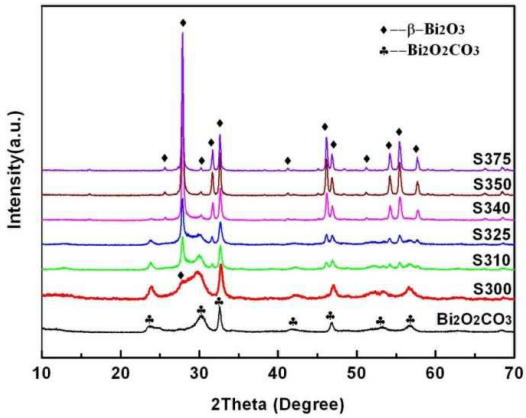


Fig. 2 XRD patterns of $Bi_2O_2CO_3$, $\beta$-$Bi_2O_3$ and $\beta$-$Bi_2O_3$/$Bi_2O_2CO_3$ composite photocatalysts synthesized at different calcination temperatures

### 3.2 Study of phase transformation from $Bi_2O_2CO_3$ to $\beta$-$Bi_2O_3$ by X-ray diffraction

The phase composition and crystal structure of the synthesized samples were examined by XRD. As shown in Fig. 2, all the diffraction peaks can be readily indexed to the tetragonal $Bi_2O_2CO_3$ (ICDD PDF 41-1488) and the tetragonal $\beta$-$Bi_2O_3$ (ICDD PDF 27-0050). Namely, the diffraction peaks marked with diamonds at $2\theta$ = 23.63, 30.29, 32.54, 41.93, 46.67, and 53.37 are assigned to the (011), (013), (110), (114), (020), and (121) planes of $Bi_2O_2CO_3$, respectively. The diffraction peaks indicated with clubs at $2\theta$ = 25.70, 27.94, 31.75, 32.68, 46.83, 48.36, 55.39, 57.68, 58.99, and 75.41 correspond to the (210), (201), (002), (220), (400), (410), (421), (402), (412), and (601) planes of $\beta$-$Bi_2O_3$, respectively. The XRD patterns of the $\beta$-$Bi_2O_3$/$Bi_2O_2CO_3$ composite photocatalysts (S300-S340) confirm the coexistence of both $Bi_2O_2CO_3$ and $\beta$-$Bi_2O_3$ phases. With increasing the calcination temperature, the intensities of the diffraction peaks of $\beta$-$Bi_2O_3$ increased continuously, whereas those of $Bi_2O_2CO_3$ decreased simultaneously, indicating that the $Bi_2O_2CO_3$ phase was partially transformed into the $\beta$-$Bi_2O_3$ phase. However, when the calcination temperature was further increased to 350°C, the diffraction peaks of $Bi_2O_2CO_3$ were nearly disappeared, suggesting that the $\beta$-$Bi_2O_3$ is the major phase in the S350. The quantitative XRD analysis of $Bi_2O_2CO_3$ and $\beta$-$Bi_2O_3$ in the $\beta$-$Bi_2O_3$/$Bi_2O_2CO_3$ composite photocatalysts was performed on multi-phase patterns by the RIR method [40-42], and the results are listed in Table 1. The average crystallite sizes of $Bi_2O_2CO_3$ and $\beta$-$Bi_2O_3$ were estimated to be 26 nm and 41 nm, respectively, by considering the most intense diffraction peaks, using the Scherrer equation, $D = 0.89\lambda/\beta\cos\theta$, where $D$, $\lambda$, $\beta$, and $\theta$ are crystallite size, Cu K$\alpha$ wavelength, full width at half maximum (FWHM) intensity, and Bragg's diffraction angle, respectively. The average crystallite sizes of $Bi_2O_2CO_3$ and $\beta$-$Bi_2O_3$ in the $\beta$-$Bi_2O_3$/$Bi_2O_2CO_3$ composite photocatalysts synthesized at 300°C, 310°C, 325°C, 340°C, 350°C, and 375°C were also calculated and summarized in Table 1. One can easily notice that with increasing the calcination temperature, the average crystallite size of $\beta$-$Bi_2O_3$ increased from 28 nm to 41 nm.

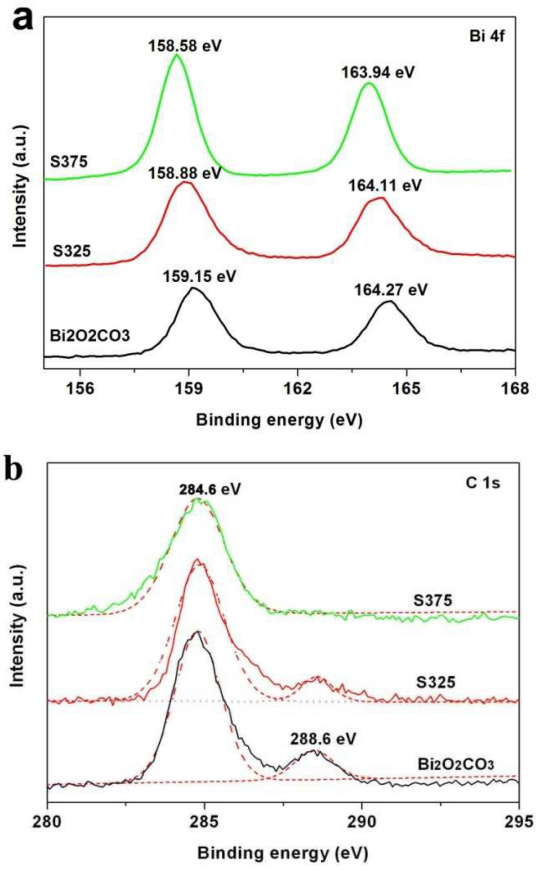


Fig. 3 XPS spectra of (a) Bi 4f and (b) C 1s of $Bi_2O_2CO_3$, S325 and S375 samples

### 3.3 Investigation of $Bi_2O_2CO_3$, $\beta$-$Bi_2O_3$ and $\beta$-$Bi_2O_3$/$Bi_2O_2CO_3$ by X-ray photoelectron spectroscopy

To elucidate the elemental compositions and chemical states of Bi and C in $Bi_2O_2CO_3$, S325 and 375 samples, the XPS analysis was performed. Fig. 3a shows the XPS spectra of Bi 4f with double peaks at binding energies of 159.2 eV and 164.2 eV, corresponding to Bi $4f_{7/2}$ and Bi $4f_{5/2}$ of $Bi_2O_2CO_3$, respectively. However, the binding energies of Bi 4f shifted towards lower energies after calcining $Bi_2O_2CO_3$ at 325°C and 375°C, that is, 159.0 eV to 158.9 eV for Bi $4f_{7/2}$ and 164.0 eV to 163.9 eV for Bi $4f_{5/2}$, which are consistent with the previously reported data for bismuth oxide [30]. Besides, the shift of binding energies confirms the complete phase transformation from $Bi_2O_2CO_3$ to $\beta$-$Bi_2O_3$ after calcination at 375°C. The XPS peak for C 1s (Fig. 3b) at 284.6 eV is ascribed to the adventitious hydrocarbon, whereas the XPS peak at 288.6 eV is attributed to the carbonate ion in $Bi_2O_2CO_3$ [43, 44]. With increasing the calcination temperature,

the XPS peak at 288.6 eV disappeared, indicating the complete phase transformation from $Bi_2O_2CO_3$ to $\beta$-$Bi_2O_3$.

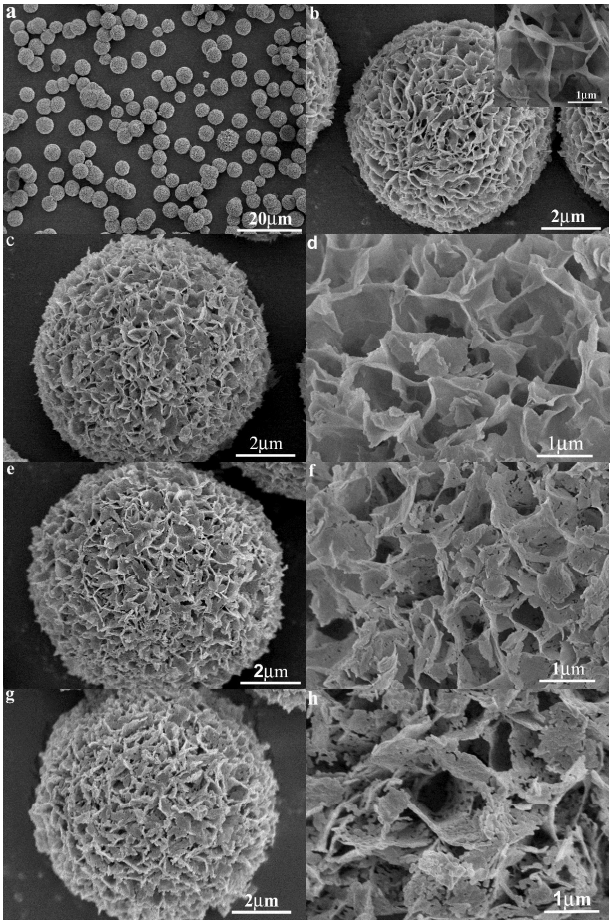


Fig. 4 SEM images of (a,b) $Bi_2O_2CO_3$, (c,d) S300, (e,f) S325, and (g,h) S350 samples

### 3.4 Effect of calcination temperature on morphology and crystal structure

The morphologies of $Bi_2O_2CO_3$, S300, S325, and S350 samples were observed by SEM, and the results are shown in Fig. 4. As shown in Fig. 4a, majority of $Bi_2O_2CO_3$ particles are uniform porous microspheres with the diameter of 4-8 μm. The magnified SEM image of a single porous microsphere shows that each porous microsphere is constructed by self-assembly of nanosheets with the thickness of *ca.* 10-20 nm (Fig. 4b). When the $Bi_2O_2CO_3$ powders were calcined at 300°C, the overall morphologies of microspheres did not change except the formation of some small pores in nanosheets (Figs. 4c and d). After calcination at 325°C and 350°C, the number of small pores in the nanosheets has significantly increased (Figs. 4e-h) due possibly to the release of $CO_2$ if not because of lattice condensation process due to the phase transformation. It can be concluded that the $\beta$-$Bi_2O_3$/$Bi_2O_2CO_3$ composite photocatalysts retained the original microspherical shape of $Bi_2O_2CO_3$ precursor. That means the $\beta$-$Bi_2O_3$ crystals were in situ formed and have an intimate contact with $Bi_2O_2CO_3$ crystals, which can efficiently facilitate the transfer of photo-generated charge carriers.

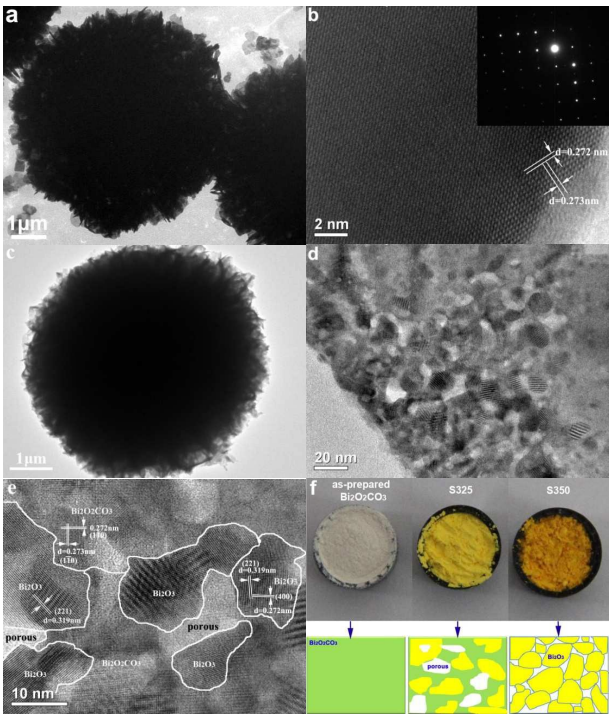


Fig. 5 TEM (a,c,d) and HRTEM (b,e) images of $Bi_2O_2CO_3$ and $\beta$-$Bi_2O_3$/$Bi_2O_2CO_3$ composite photocatalyst (S325). Digital photos of $Bi_2O_2CO_3$, S325 and S350 samples and schematic illustration of the phase transformation from $Bi_2O_2CO_3$ to $\beta$-$Bi_2O_3$/$Bi_2O_2CO_3$ (f)

The detailed structural characteristics of the $Bi_2O_2CO_3$ and $\beta$-$Bi_2O_3$/$Bi_2O_2CO_3$ composite photocatalyst synthesized at 325°C were further studied by TEM, and the results are shown in Fig. 5. The TEM image shown in Fig. 5a evidences that each sphere-like microstructure is composed of nanosheets with the thickness of about 10-20 nm. The HRTEM image of an individual nanosheet of sphere-like $Bi_2O_2CO_3$ microstructure is shown in Fig. 5b. The crystal lattice fringes are clearly observed, and the average distances between the neighboring lattice fringes are about 0.273 and 0.272 nm that correspond to the distances between the (110) and $(\bar{1}10)$ planes of tetragonal $Bi_2O_2CO_3$. The intersection angle between the (110) and $(\bar{1}10)$ planes is 90°, depicting that the **Error! Reference source not found.**$Bi_2O_2CO_3$ single crystal in the form of nanosheet has the exposed {001} facet. The SAED pattern (inset in Fig. 5b) also confirms the single-crystalline nature of the $Bi_2O_2CO_3$ nanosheets and their preferred crystal growth orientation of [001].

Fig. 5c shows the TEM image of the $\beta$-$Bi_2O_3$/$Bi_2O_2CO_3$ composite photocatalyst, revealing that the composite retained the original sphere-like morphology of $Bi_2O_2CO_3$. The pores formed during the phase transformation can be clearly seen in the magnified TEM image of a single $\beta$-$Bi_2O_3$/$Bi_2O_2CO_3$ nanosheet (S325) (Fig. 5d), which is in good agreement with the SEM data shown above. In Fig. 5e, the HRTEM image of the $\beta$-$Bi_2O_3$/$Bi_2O_2CO_3$ composite photocatalyst (S325) shows some distinct regions with different crystal lattice fringes. The neighboring lattice fringes are about 0.273 and 0.272 nm corresponding to the distances between the (110) and $(\bar{1}10)$ planes of tetragonal $Bi_2O_2CO_3$, respectively, whereas the neighboring lattice fringes with 0.319 and 0.272 nm are related to

the (221) and (400) planes of $\beta$-$Bi_2O_3$, respectively. The HRTEM results conclude that the *p-n* heterojunction was formed in the $\beta$-$Bi_2O_3$/$Bi_2O_2CO_3$ composite photocatalyst.

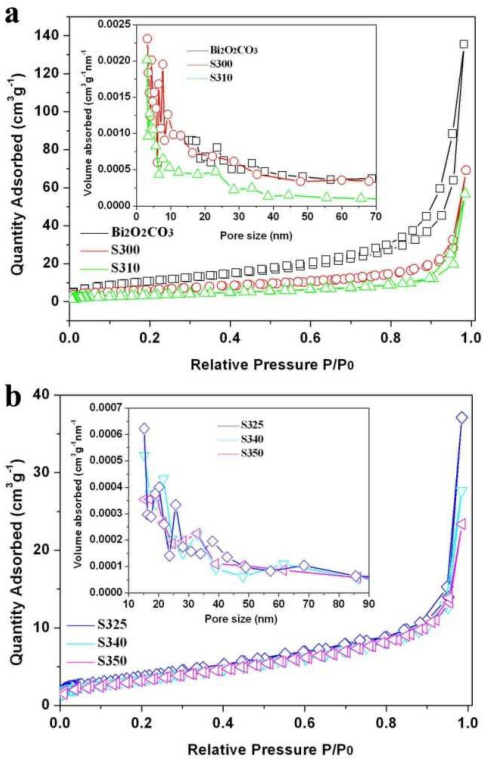


Fig. 6 $N_2$ gas adsorption-desorption isotherms and pore size distributions of $Bi_2O_2CO_3$, S300, S310, S325, S340, and S350 samples

### 3.5 Effect of calcination temperature on specific surface area

The $N_2$ gas adsorption-desorption isotherms and pore size distributions of the $Bi_2O_2CO_3$, S300, S310, S325, S340, and S350 samples are shown in Fig. 6. The specific surface areas ($S_{BET}$) measured are 32.09, 22.06, 10.45, 9.57, 8.54, and 8.41 $m^2/g$ for $Bi_2O_2CO_3$, S300, S310, S325, S340, and S350 samples, respectively. The larger specific surface area is considered to be beneficial for the enhancement of photocatalytic activity of the samples. Although the $S_{BET}$ values of the $\beta$-$Bi_2O_3$/$Bi_2O_2CO_3$ composite photocatalysts are less than that of $Bi_2O_2CO_3$, an enhancement in the photocatalytic activity is anticipated because of the formation of a *p-n* heterojunction.

### 3.6 Optical absorption properties of the synthesized samples

Fig. 7 shows the UV-Vis absorption spectra of $Bi_2O_2CO_3$, S300, S310, S325, S340, S350, and S375 samples. As shown, pure $Bi_2O_2CO_3$ can only absorb UV light ($\lambda \leq 370$ nm), while $\beta$-$Bi_2O_3$ can absorb part of visible light ($\lambda \leq 550$ nm) as well. Therefore, the $\beta$-$Bi_2O_3$/$Bi_2O_2CO_3$ composite photocatalysts have a mixed absorption property of $Bi_2O_2CO_3$ and $\beta$-$Bi_2O_3$. With increasing the $\beta$-$Bi_2O_3$ content in the composite photocatalyst, an apparent red-shift is noted. The optical band gap energies of samples were calculated using the formula (3) based on the measured absorption spectra:

$$\alpha h\upsilon = A(h\upsilon - E_g)^{n/2} \quad (3)$$

where $\alpha$, $h$, $\upsilon$, $E_g$, and $A$ are absorption coefficient, Plank constant, light frequency, band gap energy, and a constant, respectively. The $n$ is determined from the type of optical transition of a semiconductor ($n = 1$ for direct transition and $n = 4$ for indirect transition). For $Bi_2O_2CO_3$ and $\beta$-$Bi_2O_3$, the $n$ value is 4. The $E_g$ values of $Bi_2O_2CO_3$, $\beta$-$Bi_2O_3$, and S325 samples were determined to be 3.10, 2.21, and 2.35 eV, respectively, from the plot of $(\alpha h\upsilon)^{1/2}$ versus $h\upsilon$, shown in the inset of Fig. 7. The $E_g$ values of the S300, S310, S325, S340, and S350 samples are summarized in Table 1. All the composite photocatalysts have smaller $E_g$ values compared with pure $Bi_2O_2CO_3$, implying that the synthesized composite photocatalysts are more efficient in absorbing visible light than pure $Bi_2O_2CO_3$.

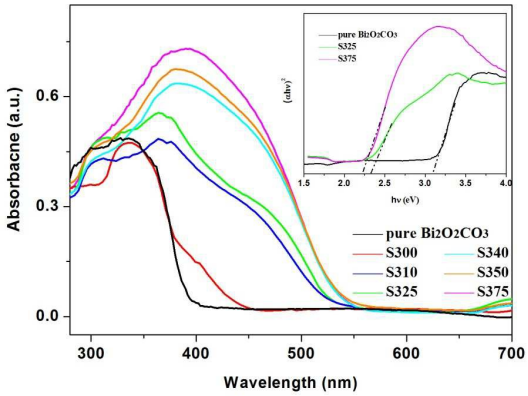


Fig. 7 UV-Vis absorption spectra and $(\alpha E_{photon})^{1/2}$ vs. $E_{photon}$ curves of $Bi_2O_2CO_3$, S300, S310, S325, S340, S350, and S375 samples

### 3.7 Photocatalytic activity of the synthesized samples for the degradation of MO, MB and phenol

To investigate the photocatalytic efficiency of the synthesized samples, the photodegradation experiments were conducted with 1.0 g/L photocatalyst and 10 mg/L MO initial concentration under 300W Xenon lamp irradiation with a 400 nm cutoff filter for 32 min. Prior to visible light irradiation, the adsorption capacities of the samples were evaluated in the dark. Fig. 8 shows the adsorption and photodegradation of MO over the $Bi_2O_2CO_3$, S300, S310, S325, S340, S350, and S375 samples. As shown, the adsorption-desorption equilibrium of MO in the dark was almost established within 30 min. Although pure $Bi_2O_2CO_3$ has a higher $S_{BET}$ value compared with the composite photocatalysts, it however showed a poor MO adsorption (about 6%), whereas 48% of MO was adsorbed by S300 sample (Fig. 8a). After establishing the adsorption-desorption equilibrium of MO in the dark, the photocatalytic efficiency was evaluated with respect to the photodegradation of MO over the samples under visible light. The variation of MO concentration ($C/C_0$) with time of the samples is shown in Fig. 8b. A blank test run without any photocatalysts evidences that the MO molecules are stable under visible light irradiation. A rapid decrease in the MO concentration was realized with the presence of the $\beta$-$Bi_2O_3$/$Bi_2O_2CO_3$ composite photocatalysts. For pure $Bi_2O_2CO_3$, the total MO photodegradation could reach only 60% after 24 min of visible light irradiation. In contrast, the total MO photodegradation of the $\beta$-$Bi_2O_3$/$Bi_2O_2CO_3$ composite photocatalysts increased significantly with increasing the

calcination temperature up to 325°C and slightly declined above 325°C. Surprisingly, the complete photodegradation of MO was achieved with S325 sample within 24 min of visible light irradiation, whereas the S300, S310, S340, and S350 samples showed the total MO photodegradation of 83%, 96%, 72%, and 42%, respectively. It is believed that an increase in the calcination temperature up to 325°C facilitated the formation of more $\beta$-$Bi_2O_3$/$Bi_2O_2CO_3$ heterojunction interfaces that could suppress the recombination of photo-generated electrons and holes. Higher calcination temperatures above 325°C led to the decrease in the heterojunction interfaces that acted as recombination centers for the electron-hole pairs. Hence, due to the high recombination rate of photo-generated electron-hole pairs, pure $\beta$-$Bi_2O_3$ synthesized at 375°C showed a relatively low photocatalytic activity for the photodegradation of MO under visible light, with the total photodegradation of 34%. Fig. 8c shows the UV-Vis spectra of MO aqueous solution taken out at different reaction times during the photodegradation process with S325 sample. It is clear that with increasing the visible light irradiation time, the peak intensity of MO at around 464 nm decreased gradually and disappeared completely at 24 min.

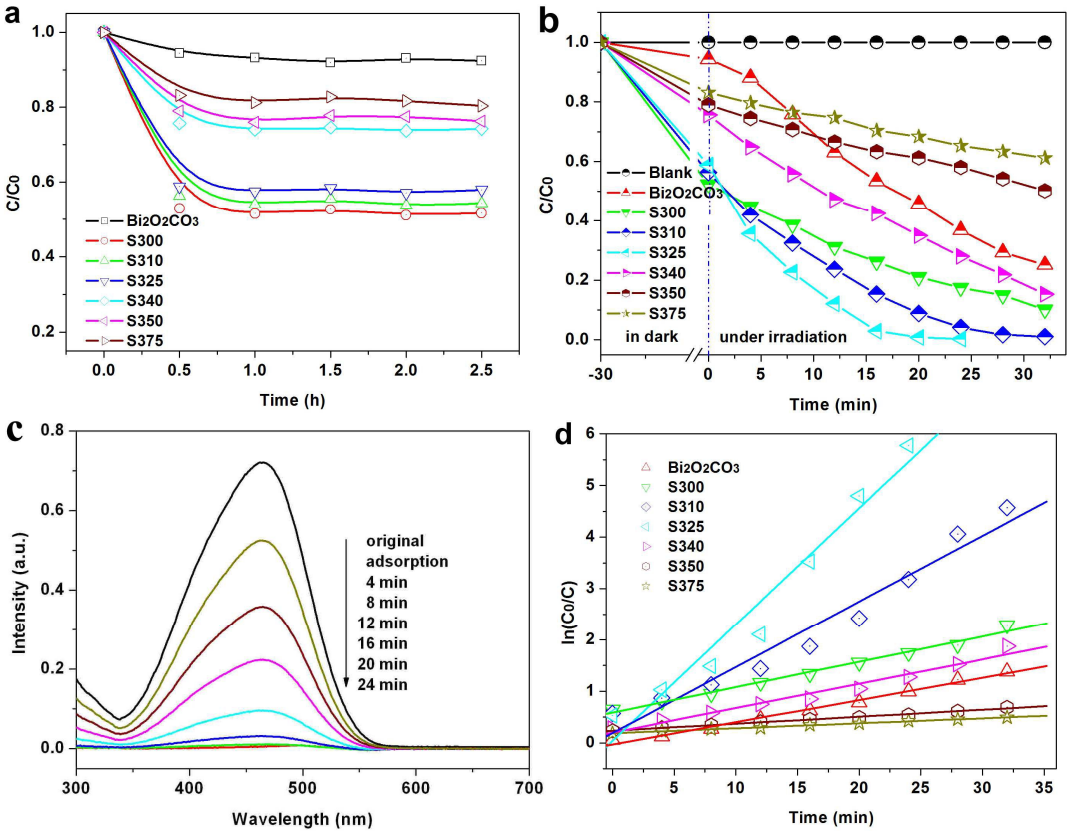


Fig. 8 Adsorption (a) and photodegradation (b) profiles of MO over the $Bi_2O_2CO_3$, S300, S310, S325, S340, S350, and S375 samples. UV-Vis spectra of MO in aqueous solution taken out at different reaction times during the photodegradation process with S325 sample (c). Kinetic linear simulation curves of MO photodegradation over the synthesized samples under visible light irradiation (d)

According to the Langmuir-Hinshelwood (L-H) kinetics model, the MO photodegradation rate over the synthesized samples can be expressed using the following apparent pseudo-first-order kinetics equation (4):

$$\ln C_0/C = kt \quad (4)$$

where $k$ is the apparent pseudo-first-order rate constant ($min^{-1}$), $C$ is the MO concentration in aqueous solution at time $t$ (mg/L), $C_0$ is the initial MO concentration (mg/L). The calculated $k$ values of the synthesized samples are given in Table 1. The S325 sample showed the highest $k$ value with the best photocatalytic activity, whereas the S375 (bare $\beta$-$Bi_2O_3$) sample showed the lowest $k$ value. Compared with S300, S340, and S350 samples with the $k$ values of 0.0628, 0.0482, and 0.0472 $min^{-1}$, respectively, the S310 and S325 samples with the $k$ values of 0.0784 $min^{-1}$ and 0.0676 $min^{-1}$, respectively, showed higher photocatalytic activities. This observation can be explained by the formed $p$-$n$ heterojunction at the interfaces of $\beta$-$Bi_2O_3$ and $Bi_2O_2CO_3$ crystals. That is, at lower calcination temperatures, there were less $\beta$-$Bi_2O_3$/$Bi_2O_2CO_3$ heterojunctions formed because of lower content of $\beta$-$Bi_2O_3$ converted, limiting the separation of electrons and holes. On the contrary, at higher calcination temperatures, there were also less $\beta$-$Bi_2O_3$/$Bi_2O_2CO_3$ heterojunctions formed because of lower content of $Bi_2O_2CO_3$, which was ultimately converted to $\beta$-$Bi_2O_3$. Thus, finding an appropriate ratio of $Bi_2O_2CO_3$ to $\beta$-$Bi_2O_3$ in the $\beta$-$Bi_2O_3$/$Bi_2O_2CO_3$ composite photocatalyst was essential to achieve higher photocatalytic performance.

Also, the dye concentration has a significant effect on the evaluation of photocatalytic efficiency of the photocatalysts. Fig. 9 shows the influence of initial MO concentration on its total photodegradation over S325 sample. As expected, the lower initial MO concentration leads to the higher photodegradation efficiency. It is thought that the MO photodegradation may be governed by the limited number of surface active sites of the

photocatalyst. However, MO can be completely decomposed within 3 h under visible light irradiation even using the high initial MO concentration of 40 mg/L in this work. These results indicate that the as-synthesized $\beta$-$Bi_2O_3$/$Bi_2O_2CO_3$ composite photocatalyst shows better photocatalytic activity for the photodegradation of anionic MO molecules.

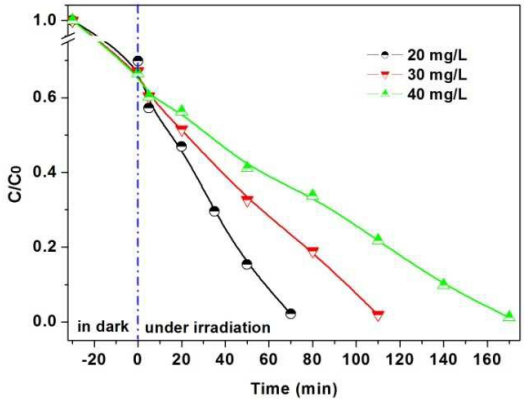


Fig. 9 Photodegradation profiles of MO with different initial concentrations over S325 sample

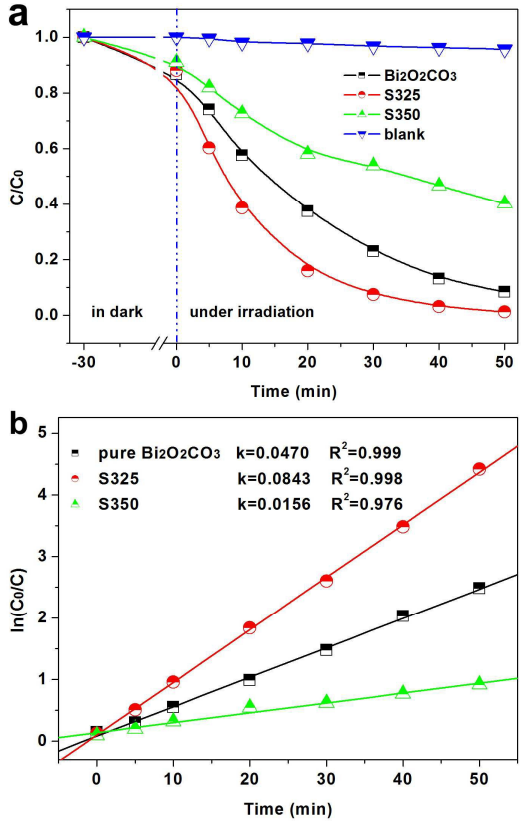


Fig. 10 (a) Photodegradation profiles of MB over $Bi_2O_2CO_3$, S325 and S350 samples ($C_0$ = 10 mg/L, photocatalyst = 1 g/L). (b) Kinetic linear simulation curves of MB photodegradation with different samples

We have also studied the photocatalytic efficiency of the synthesized samples for the photodegradation of cationic dye, MB, under visible light irradiation. Fig. 10a shows the photodegradation profiles of MB over $Bi_2O_2CO_3$, S325, and S350 samples. As shown, the photodegradation of MB over S325 sample is much higher than over $Bi_2O_2CO_3$ and S350 samples. The complete photodegradation of MB was achieved with S325 sample within 50 min of visible light irradiation, whereas the pure $Bi_2O_2CO_3$ and S350 samples showed the total MB photodegradation of 91% and 59%, respectively. The pseudo-first-order reaction rate constants were calculated by plotting kinetic linear simulation curves of MB photodegradation with different samples shown in Fig. 10b.

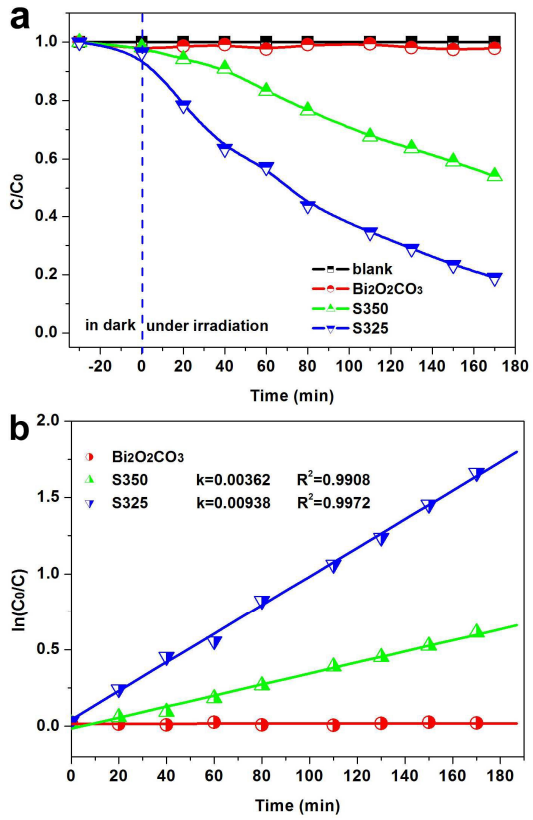


Fig. 11 (a) Photodegradation profiles of phenol over $Bi_2O_2CO_3$, S325 and S350 samples ($C_0$ = 0.2 mmol/L, photocatalyst = 1 g/L). (b) Kinetic linear simulation curves of phenol photodegradation with different samples

MO and MB studied in this work as target pollutants are typical color dyes. In order to extend the use of the synthesized $\beta$-$Bi_2O_3$/$Bi_2O_2CO_3$ composite photocatalyst, phenol was also tested as a colorless pollutant. The photodegradation profiles of phenol over the $Bi_2O_2CO_3$, S325 and S350 samples are shown in Fig. 11. It is known that photo-generated holes can directly react with molecules of various organic pollutants owing to their strong oxidation ability, and they are almost nonselective for the reaction with pollutants. Phenol is considered to be one of the highly toxic pollutants that can cause serious environmental problems and are harmful to human beings. According to Xie et al. [45], holes played a major role in the photodegradation of phenol over $BiVO_4$ under visible light irradiation. The effective photodegradation of organic dyes (Fig. 8) and phenol (Fig. 11) by $\beta$-$Bi_2O_3$/$Bi_2O_2CO_3$ and $\beta$-$Bi_2O_3$ samples also confirms their conclusion. The photodegradation experiments performed without $Bi_2O_2CO_3$ (Fig. 11) showed no obvious change in phenol concentration within 170 min of the reaction under visible light irradiation. However, the photodegradation of phenol over $\beta$-

$Bi_2O_3/Bi_2O_2CO_3$ and $\beta$-$Bi_2O_3$ samples was found to be 81% and 42%, respectively, after 170 min under visible light irradiation. In all cases, the photodegradation of MO, MB and phenol over $\beta$-$Bi_2O_3/Bi_2O_2CO_3$ composite photocatalyst was much higher than that over the pure $Bi_2O_2CO_3$ and $\beta$-$Bi_2O_3$ samples due to the combination of the two photocatalysts that were simultaneously involved in strong oxidation reactions under visible light irradiation. Therefore, the synthesized $\beta$-$Bi_2O_3/Bi_2O_2CO_3$ composite photocatalyst with high photocatalytic performance will be beneficial for the environmental applications.

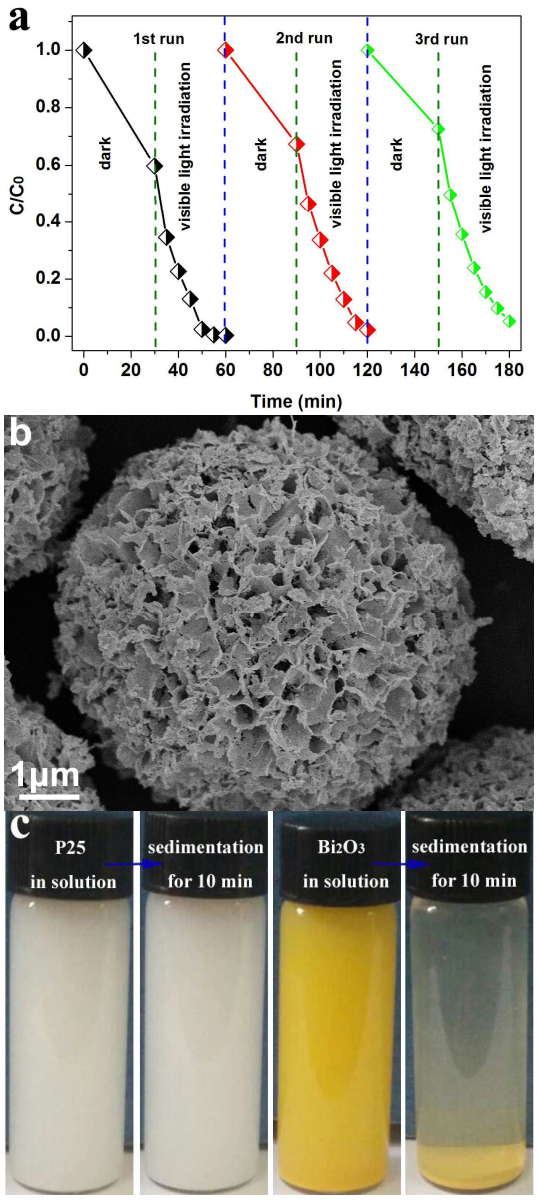


Fig. 12 (a) Photodegradation profiles of MO over S325 composite photocatalyst after three cycles of photodegradation reaction, (b) SEM image of S325 composite photocatalyst after three cycles of photodegradation reaction, and (c) photographs of solutions with P25-$TiO_2$ and S325 samples before and after sedimentation for 10 min.

Recycling and maintaining of chemical stability and high photocatalytic activity are critical issues for the long-term application of the composite photocatalyst. As known, the photocorrosion or photodissolution of photocatalysts may occur on the photocatalyst surface during the photocatalytic reaction. To determine the stability of S325 sample for the degradation of MO under visible light, the photocatalyst powders were collected after the photodegradation reaction, dried, and reused for three times under the identical experimental conditions. The results are plotted in Fig. 12a. After three cycles, the S325 composite photocatalyst still maintains higher photodegradation efficiency. Also, to confirm the morphological stability of the S325 composite photocatalyst particles, the photocatalyst powders collected after three cycles were examined by SEM. As shown in SEM image (Fig. 12b), the S325 composite photocatalyst after three cycles of photodegradation reaction still preserves its spherical porous structure. The results shown in Fig. 12c indicate that the S325 composite photocatalyst can easily be separated from aqueous suspension by sedimentation due to the high density of $\beta$-$Bi_2O_3$ particles (8.9 g/cm$^3$) compared with that of P25-$TiO_2$ (4.2 g/cm$^3$). Therefore, the $\beta$-$Bi_2O_3/Bi_2O_2CO_3$ composite photocatalyst shows a highly efficient photocatalytic activity for the degradation of organic pollutants under visible light irradiation along with its easy recyclability.

Considering its absorption edge shown in Fig. 7, pure $Bi_2O_2CO_3$ can only absorb light < 380 nm. Hence, visible light ($\lambda \geq 420$ nm) can not completely excite $Bi_2O_2CO_3$ to generate reactive radicals because of its wide band gap. Therefore, the photodegradation of MO over pure $Bi_2O_2CO_3$ through a photocatalytic pathway is expected to be negligible. Nevertheless, 60% MO was degraded by pure $Bi_2O_2CO_3$ under visible light irradiation for 24 min (Fig. 8). The dye photodegradation mechanisms of $Bi_2O_2CO_3$ through the photosensitization pathway under visible light irradiation have been previously reported [4]. More importantly, on the preferentially exposed {001} facet of the $Bi_2O_2CO_3$ nanosheets, the Bi–O square antiprism with [8]–coordination compressed along the *c*-axis provides lots of defects formed from unstable oxygen having an unstable bond with the Bi atoms in the $Bi_2O_2CO_3$ crystal structure [17]. Furthermore, a thin thickness of nanosheets also contributes to the distortion of the Bi–O polyhedron, in which electron-hole pairs generated inside the crystal can easily travel to the surface and react with MO molecules. Therefore, the pure $Bi_2O_2CO_3$ with the band gap of about 3.1 eV could also exhibit a good visible-light-driven photodegradation efficiency. Similar results were also reported for another important wide-band gap semiconductor BiOCl [46].

### 3.8 Role of scavengers in the photodegradation of organic pollutants over the synthesized samples

In the photocatalytic oxidation process of dyes molecules, a series of photo-generated reactive species, including •OH, $\bullet O^{2-}$ or $h^+$, will directly take part after electron-hole pairs are generated upon light irradiation [47]. As Chen et al. [19] described, the photodegradation of MB over the $Bi_2O_2CO_3$/BiOI composite phototocatalyst was mainly due to the presence of •OH. It was also suggested that $h^+$ and $\bullet O^{2-}$ play a major role in the photodegradation of MO over the BiOI/$(BiO)_2CO_3$ system under visible light irradiation [48]. To evaluate the role of each reactive species in the photodegradation of MO over the S325 sample, some scavengers and $N_2$ purging without adding any scavengers

were employed. In this study, benzoquinone, isopropyl alcohol, and ammonium oxalate were adopted as traps for $\bullet O^{2-}$, •OH, and $h^+$, respectively. Fig. 13 shows the photodegradation profiles of MO over the S325 sample with different scavengers and $N_2$ purging. As shown, after the addition of benzoquinone or ammonium oxalate, the photodegradation of MO was inhibited significantly, giving only 60% and 48% MO photodegradation within 60 min of visible light irradiation. This evidences that $\bullet O^{2-}$ and $h^+$ also contributed to the overall photodegradation of MO over the $\beta$-$Bi_2O_3$/$Bi_2O_2CO_3$ composite photocatalyst under visible light irradiation. The reactive $\bullet O^{2-}$ could also be generated through the reaction between photo-generated electrons and $O_2$ adsorbed on the surface of the $\beta$-$Bi_2O_3$/$Bi_2O_2CO_3$ composite photocatalyst. The reduced photocatalytic activity of the $\beta$-$Bi_2O_3$/$Bi_2O_2CO_3$ composite photocatalyst under $N_2$ purging without any scavengers connotes that $O_2$ primarily acted as an efficient electron trap, leading to the generation of $\bullet O^{2-}$ and preventing the recombination of electrons and holes. Interestingly, the addition of isopropyl alcohol showed a weak effect on the photocatalytic oxidation of MO, suggesting that the contribution of •OH was negligible to the overall photodegradation of MO over the $\beta$-$Bi_2O_3$/$Bi_2O_2CO_3$ composite photocatalyst under visible light irradiation.

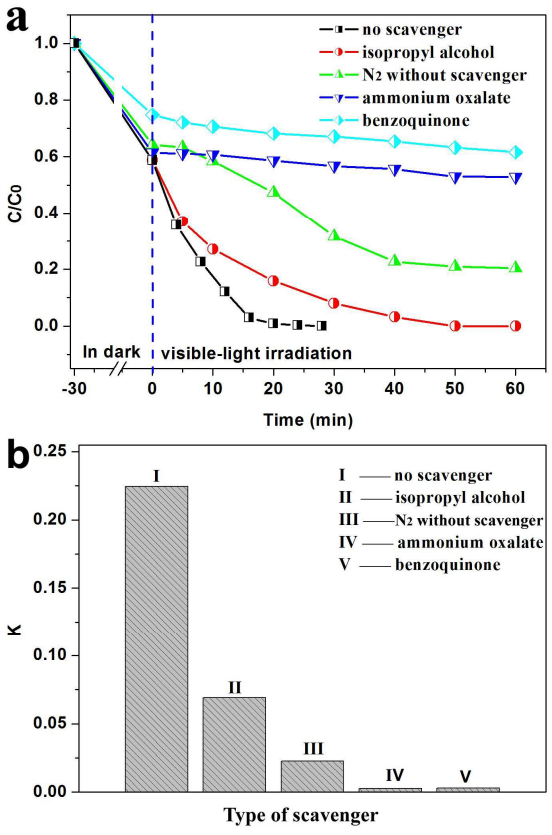


Fig. 13 (a) Photodegradation profiles of MO over the S325 sample with different scavengers and $N_2$ purging and (b) apparent pseudo-first-order rate constants ($k$)

### 3.9 Photodegradation mechanisms of organic pollutants over the synthesized samples

Considering the results shown in Fig. 8b, the $\beta$-$Bi_2O_3$/$Bi_2O_2CO_3$ composite photocatalyst demonstrated higher photocatalytic activity than individual $\beta$-$Bi_2O_3$ or $Bi_2O_2CO_3$. It is believed that the enhancement of photocatalytic activity of composite photocatalyst is mainly attributed to the efficient charge transfer at the *p-n* heterojunction formed between $Bi_2O_2CO_3$ and $\beta$-$Bi_2O_3$ with matching band potentials, which consequently favors an effective separation of photo-generated electron-hole pairs. The charge carriers can transfer from the bulk to the surface of the photocatalyst to react with the molecules of the adsorbed reactants. Fig. 14a shows the transient photocurrent responses measured for $Bi_2O_2CO_3$, S325, and S375 samples. It is obvious that the photocurrent intensity of pure $Bi_2O_2CO_3$ under visible light irradiation is insignificant, whereas the photocurrent intensity of the S325 sample is nearly 2.5 times higher than that of S375. This indicates that more effective separation of photo-induced electrons and holes and a faster interfacial charge transfer took place at the *p-n* heterojunction of composite photocatalyst, enhancing the photocatalytic activity. Based on the energy band structure of the $\beta$-$Bi_2O_3$/$Bi_2O_2CO_3$ composite photocatalyst and the effects of scavengers, a possible mechanistic pathway for the enhanced photocatalytic activity of the $\beta$-$Bi_2O_3$/$Bi_2O_2CO_3$ composite photocatalyst is also proposed here.

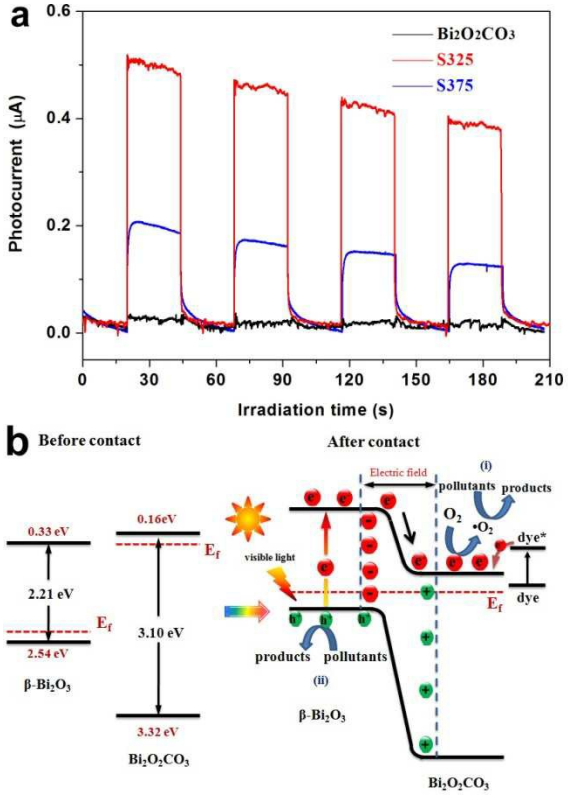


Fig. 14 (a) Transient photocurrent responses for $Bi_2O_2CO_3$, S325, and S375 samples and (b) the formation of $\beta$-$Bi_2O_3$/$Bi_2O_2CO_3$ *p-n* heterojunction and possible charge separation process

The energy band structures of $\beta$-$Bi_2O_3$ and $Bi_2O_2CO_3$ are schematically illustrated in Fig. 14b (*left*). Comparing the CB and VB positions of $Bi_2O_2CO_3$ and $\beta$-$Bi_2O_3$, it seems that the nested band structure is unfavorable for the separation of photo-generated charge carriers. It is believed that when the two semiconductors are in contact, the *p-n* heterojunction is formed at the interfaces of $\beta$-$Bi_2O_3$ and $Bi_2O_2CO_3$, and the CB and VB

positions of $Bi_2O_2CO_3$ and $\beta$-$Bi_2O_3$ change to reach equilibration of Fermi levels ($E_f$) of $Bi_2O_2CO_3$ and $\beta$-$Bi_2O_3$. Hence, there is a diffusion of electrons from $Bi_2O_2CO_3$ to $\beta$-$Bi_2O_3$, resulting in the accumulation of negative charges in the $\beta$-$Bi_2O_3$ side close to the *p-n* heterojunction. Meantime, holes transfer from $\beta$-$Bi_2O_3$ to $Bi_2O_2CO_3$, leaving a positive section in the $Bi_2O_2CO_3$ side near the *p-n* heterojunction. With the equilibration of Fermi level in the $\beta$-$Bi_2O_3$/$Bi_2O_2CO_3$ composite photocatalyst, the diffusion of electrons from $Bi_2O_2CO_3$ to $\beta$-$Bi_2O_3$ stops and the energy bands of $\beta$-$Bi_2O_3$ shift upward along the Fermi level ($E_{fp}$) and those of $Bi_2O_2CO_3$ shift downward along the Fermi level ($E_{fn}$), as shown in Fig. 14b (*right*). Under visible light irradiation, only $\beta$-$Bi_2O_3$ in the $\beta$-$Bi_2O_3$/$Bi_2O_2CO_3$ composite photocatalyst can be excited and electron-hole pairs are generated. With the effect of inner electric field at the *p-n* heterojunction, the photo-generated electrons move to the positive field (*n*-type $Bi_2O_2CO_3$) and react with $O_2$ adsorbed on the surface of the $\beta$-$Bi_2O_3$/$Bi_2O_2CO_3$ composite photocatalyst to produce reactive $\bullet O^{2-}$ with strong oxidation property that further degrade the molecules of MO and MB. Meantime, the photo-generated holes migrate to the negative field (*p*-type $\beta$-$Bi_2O_3$) and directly oxidize the molecules of dyes or phenol in the reaction solution. In such a way, the photo-generated electron-hole pairs will be separated effectively by a *p-n* heterojunction formed in the $\beta$-$Bi_2O_3$/$Bi_2O_2CO_3$ composite photocatalyst. Therefore, the $\beta$-$Bi_2O_3$/$Bi_2O_2CO_3$ composite photocatalyst can exhibit an enhanced photocatalytic activity compared with $Bi_2O_2CO_3$ and $\beta$-$Bi_2O_3$ for the photodegradation of organic pollutants under visible light. Similarly, we have also demonstrated previously the enhanced photocatalytic activities of $Co_3O_4$/BiOCl [6], $Fe_3O_4$/$Bi_2O_2CO_3$ [15], and $TiO_2$/BiOCl [49] composite photocatalysts for the photodegradation of dye molecules under visible light.

## 4. Conclusions

In summary, porous $\beta$-$Bi_2O_3$/$Bi_2O_2CO_3$ composite photocatalysts with a *p-n* heterojunction were successfully fabricated through a simple thermodecomposition process in the temperature range of 300-375°C of porous sphere-like $Bi_2O_2CO_3$ hierarchitectures with the exposed {001} facets synthesized hydrothermally. Without any expensive metal components and co-catalysts, the as-synthesized $\beta$-$Bi_2O_3$/$Bi_2O_2CO_3$ composite photocatalysts exhibited enhanced photocatalytic activities for the decomposition of methyl orange, methylene blue and phenol as model organic pollutants under visible light irradiation compared with $Bi_2O_2CO_3$ and $\beta$-$Bi_2O_3$ due to the *p-n* heterojunction formed at the interfaces of $\beta$-$Bi_2O_3$ and $Bi_2O_2CO_3$.

## Notes and references

[a] *School of Physics and Information Technology, Shaanxi Normal University, Xi'an 710062, PR China. Fax: +86 29 81530750; Tel: +86 29 81530750; E-mail: zgq2006@snnu.edu.cn*

[b] *Department of Natural and Mathematic Sciences, Turin Polytechnic University in Tashkent, Kichik Halqa Yo'li 17, Tashkent 100095, Uzbekistan; E-mail: hmirabbos@gmail.com*

[c] *Facultad de Ciencias, Universidad Nacional de Ingeniería, P.O. Box 31-139, Av. Tupac Amaru 210, Lima 31, Perú; E-mail: jrodriguez@uni.edu.pe*

[d] *Instituto de Química Física de los Materiales, Medio Ambiente y Energía (INQUIMAE), Facultad de Ciencias Exactas y Naturales, Universidad de Buenos Aires, Pabellón II, Ciudad Universitaria, C1428EHA-Buenos Aires, Argentina; E-mail: saraaldabe@gmail.com*

## Acknowledgments

This work was supported by the National Natural Science Foundation of China (Program nos. 51102160, 51272148 and 51302162), the Fundamental Research Funds for the Central Universities (Grant nos. GK201402009, GK201401003 and GK201501004) and College Students' Innovative Projects of the State Ministry of Education (Program no. 201410718013). MH would like to thank the World Academy of Sciences (TWAS) for awarding a TWAS-UNESCO Associateship.

[1] X. Xiang, L.S. Xie, Z.W. Li, and F. Li. Chem. Eng. J. 221 (2013) 222–229.
[2] Y.N. Zhang, H.Q. Fan, M.M. Li and H.L. Tian. Dalton Trans. 42 (2013) 13172–13178.
[3] J.G. Hou, Z. Wang, S.Q. Jiao, H.M. Zhu. CrystEngComm. 14 (2012) 5923–5928.
[4] W.Z. Wang, X.W. Huang, S.A. Wu, Y.X. Zhou, L.J. Wang, H.L. Shi, Y.J. Liang, B. Zou. Appl. Catal. B: Environ. 134-135 (2013) 293–301.
[5] D. Sarkar, C.K. Ghosh, S. Mukherjee, K.K. Chattopadhyay. ACS Appl. Mater. Interfaces 5 (2013) 331–337.
[6] C.W. Tan, G.Q. Zhu, M. Hojamberdiev, K. Okada, J. Liang, X.C. Luo, P. Liu, Y. Liu. Appl. Catal. B: Environ. 152-153 (2014) 425–436.
[7] S.S. Yi, X.Z. Yue, D.D. Xu, Z.P. Liu, F. Zhao, D.J. Wang, Y.H. Lin. New J. Chem. 39 (2015) 2917-2924.
[8] J. Chen, S.H. Shen, P.H. Guo, M. Wang, P. Wu, X.X. Wang L.J. Guo. Appl. Catal. B: Environ. 152-153 (2014) 335–341.
[9] D. Hao, Z.M. Yang, C.H. Jiang, J.S. Zhang. Appl. Catal. B: Environ. 144 (2014) 196–202.
[10] J.D. Grice. Can. Mineral. 40 (2002) 693–698.
[11] X.Y. Chen, H.S. Huh, S.W. Lee. J. Solid. State. Chem. 180 (2007) 2510–2516.
[12] R. Chen, M.H. So, J. Yang, F. Deng, C.M. Che, H.Z. Sun. Chem. Commun. 21 (2006) 2265–2267.
[13] H.F. Cheng, B.B. Huang, K.S. Yang, Z.Y. Wang, X.Y. Qin, X.Y. Zhang, Y. Dai. ChemPhysChem 11(2010) 2167–2173.
[14] Y.Y. Liu, Z.Y. Wang, B.B. Huang, K.S. Yang, X.Y. Zhang, X.Y. Qin, Y. Dai. Appl. Surf. Sci. 257 (2010) 172–175.
[15] G.Q. Zhu, M. Hojamberdiev, K.-i. Katsumata, X. Cai, N. Matsushita, K. Okada, P. Liu, J.P. Zhou. Mater. Chem. Phys. 142 (2013) 95–105.
[16] L. Jin, G.Q. Zhu, M. Hojamberdiev, X.C. Luo, C.W. Tan, J.H. Peng, X.M. Wei, J.P. Li, P. Liu. Ind. Eng. Chem. Res. 53 (2014) 13718–13727.
[17] Y. Zheng, F. Duan, M.Q. Chen, Y. Xie. J. Molecular Catal. A: Chem. 317 (2010) 34–40.
[18] S.J. Peng, L.L. Li, H.T. Tan, Y.Z. Wu, R. Cai, H. Yu, X. Huang, P.N. Zhu, S. Ramakrishna, M. Srinivasana, Q.Y. Yan. J. Mater. Chem. A. 1 (2013) 7630–7638.
[19] L. Chen, S.F. Yin, S.L. Luo, R. Huang, Q. Zhang, T. Hong, and P.C.T. Au. Ind. Eng. Chem. Res. 51 (2012) 6760−6768.
[20] N. Liang, M. Wang, L. Jin, S.S. Huang, W.L Chen, M. Xu, Q.Q. He, J.T. Zai, N.H. Fang, and X.F. Qian. ACS Appl. Mater. Interfaces 2014, 6, 11698−11705
[21] P. Madhusudan, J.R. Ran, J. Zhang, J.G. Yu, G. Liu. Appl. Catal. B: Environ. 110 (2011) 286–295.
[22] X. Zhang, T. Guo, X. Wang, Y. Wang, C. Fan, H. Zhang, Appl. Catal. B: Environ. 150–151 (2014) 486–495.
[23] Y.-S. Xu, W.-D. Zhang, Appl. Catal. B: Environ. 140–141 (2013) 306–316.
[24] W. Wang, H. Cheng, B. Huang, X. Lin, X. Qin, X. Zhang, Y. Dai. J. Colloid Interface Sci. 402 (2013) 34–39.
[25] X. Huang, H. Chen. Appl. Surf. Sci. 284 (2013) 843–848.
[26] H. Gan, G. Zhang, H. Huang. J. Hazard. Mater. 250–251 (2013) 131–137.
[27] A. Cabot, A. Marsal, J. Arbiol, J. R. Morante. Sensors Actuators B 99 (2004) 74–89.

[28] Y.F. Qiu, M.L. Yang, H.B. Fan, Y.Z. Zuo, Y.Y. Shao, Y.J. Xu, X.X. Yang, S.H. Yang. CrystEngComm. 13 (2011) 1843–1850.
[29] G.Q. Zhu, W.X. Que, J. Zhang. J. Alloys. Compd. 509 (2011) 9479–9486.
[30] G.Q. Zhu, J. Liang, M. Hojamberdiev, W.X. Que. J. Clust. Sci. 24 (2013) 829–841.
[31] L. Zhou, W. Wang, H. Xu, S. Sun, M. Shang. Chem. Eur. J. 15 (2009) 1776–1782.
[32] A. Hameed, V. Gombac, T. Montini, L. Felisari, P. Fornasiero. Chem. Phys. Lett. 483 (2009) 254–261.
[33] S.Y. Chai, Y.J. Kim, M.H. Jung, A.K. Chakraborty, D. Jung, W.I. Lee. J. Catal. 262 (2009) 144–149.
[34] M.L. Guan, D.K. Ma, S.W. Hu, Y.J. Chen, and S.M. Huang. Inorg. Chem. 50 (2011) 800-805.
[35] J.G. Hou, Z. Wang, S.Q. Jiao, and H.M. Zhu. CrystEngComm. 14 (2012) 5923–5928.
[36] P.R. Ren, H.Q. Fan and X. Wang. Appl. Phys. A. 111 (2013) 1139–1145.
[37] Y. Peng, M. Yan, Q.G. Chen, C.M. Fan, H.Y. Zhou, A.W. Xu. J. Mater. Chem. A. 2 (2014) 8517-8524.
[38] Y. Wang, Y.Y. Wen, H.M. Ding, Y.K. Shan. J. Mater. Sci. 45 (2010) 1385–1392.
[39] H. Liu, M. Luo, J.C. Hu, T.F. Zhou, R. Chen, J.L. Li. Appl. Catal. B: Environ. 140–141(2013)141-150.
[40] C.R. Hubbard, E.H. Evans, D.K. Smith, J. Appl. Crystallogr. 9 (1976) 169–174.
[41] A. Querejeta-Fernandez, M. Parras, A. Varela, F.D. Monte, M. Garcia-Hernandez, J.M. Gonzalez-Calbet, Chem. Mater. 22 (2010) 6529–6541.
[42] D.S. Wang, Y.D. Duan, Q.Z. Luo, X.Y. Li, L.L. Bao, Desalination 270 (2011) 174–180.
[43] P. Madhusudan, J.G. Yu, W.G. Wang, B. Cheng, G. Liu. Dalton. Trans. 41 (2012) 14345–14353.
[44] L. Chen, R. Huang, S.F. Yin, S.L. Luo, C.T. Au. Chem. Eng. J. 193–194 (2012) 123–130
[45] B.P. Xie, H.X. Zhang, P.X. Cai, R.L. Qiu, Y. Xiong. Chemosphere 63 (2006) 956–963.
[46] J. Jiang, K. Zhao, X. Xiao, L. Zhang, J. Am. Chem. Soc. 134 (2012) 4473–4476.
[47] S.J. Liang, S.Y. Zhu, Y. Chen, W.M. Wu, X.C. Wang, L. Wu. J. Mater. Chem. 22 (2012) 2670–2678.
[48] J. Cao, X. Li, H.L. Lin, S.F. Chen, X.L. Fu. J. Hazard. Mater. 239–240 (2012) 316–324.
[49] G.Q. Zhu, M. Hojamberdiev, C.W. Tan, L. Jin, C. Xu, Y. Liu, P. Liu, J.P. Zhou. Mater. Chem. Phys. 147 (2014) 1146–1156.

# Table of Contents Entry

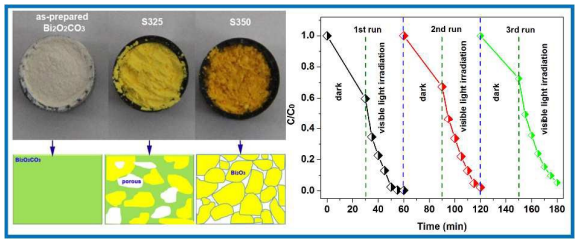


Porous $\beta$-$Bi_2O_3$/$Bi_2O_2CO_3$ composite photocatalysts showed enhanced photocatalytic activities for degrading organic pollutants under visible light due to the *p*-*n* heterojunction.